

Essay

Integrated Encapsulation and Implementation of a Linear-Mode APD Detector for Single-Pixel Imaging Lidar

Akang Lv ^{1,2,3}, Kee Yuan ^{1,3,*}, Jian Huang ^{1,3}, Dongfeng Shi ^{1,3}, Shiguo Zhang ^{1,4}, Yafeng Chen ^{1,3} and Zixin He ^{1,3}

- ¹ Kay Laboratory of Atmospheric Optics, Anhui Institute of Optics and Fine Mechanics, Hefei Institutes of Physical Science, Chinese Academy of Sciences, Hefei 230031, China; akl@mail.ustc.edu.cn (A.L.); jhuang@aiofm.ac.cn (J.H.); dfshe@aiofm.ac.cn (D.S.); zsgzsq@sina.com (S.Z.); cyfustc@mail.ustc.edu.cn (Y.C.); zhexin@aiofm.ac.cn (Z.H.)
- ² Science Island Branch of Graduate School, University of Science and Technology of China, Hefei 230026, China
- ³ Advanced Laser Technology Laboratory of Anhui Provincial, Hefei 230037, China
- ⁴ Anhui Meteorological Observation Technical Center, Hefei 230061, China
- * Correspondence: keyuan@aiofm.ac.cn

Abstract: Single-pixel imaging lidar is a novel technology that leverages single-pixel detectors without spatial resolution and spatial light modulators to capture images by reconstruction. This technique has potential imaging capability in non-visible wavelengths compared with surface array detectors. An avalanche photodiode (APD) is a device in which the internal photoelectric effect and the avalanche multiplication effect are exploited to detect and amplify optical signals. An encapsulated APD detector, with an APD device as the core, is the preferred photodetector for lidar due to its high quantum efficiency in the near-infrared waveband. However, research into APD detectors in China is still in the exploratory period, when most of the work focuses on theoretical analysis and experimental verification. This is a far cry from foreign research levels in key technologies, and the required near-infrared APD detectors with high sensitivity and low noise have to be imported at a high price. In this present study, an encapsulated APD detector was designed in a linear mode by integrating a bare APD tube, a bias power circuit, a temperature control circuit and a signal processing circuit, and the corresponding theoretical analysis, circuit design, circuit simulation and experimental tests were carried out. Then, the APD detector was applied in the single-pixel imaging lidar system. The study showed that the bias power circuit could provide the APD with an operating voltage of DC 1.6 V to 300 V and a ripple voltage of less than 4.2 mV. Not only that, the temperature control circuit quickly changed the operating state of the Thermo Electric Cooler (TEC) to stabilize the ambient temperature of the APD and maintain it at 25 ± 0.3 °C within 5 h. The signal processing circuit was designed with a multi-stage amplification cascade structure, effectively raising the gain of signal amplification. By comparison, the trial also suggested that the encapsulated APD detector and the commercial Licel detector had a good agreement on the scattered signal, such as a repetition rate and pulse width response under the same lidar environment. Therefore, target objects in real atmospheric environments could be imaged by applying the encapsulated APD detector to the near-infrared single-pixel imaging lidar system.

Keywords: single-pixel imaging; near-infrared; linear mode; APD detector; circuit design



Citation: Lv, A.; Yuan, K.; Huang, J.; Shi, D.; Zhang, S.; Chen, Y.; He, Z. Integrated Encapsulation and Implementation of a Linear-Mode APD Detector for Single-Pixel Imaging Lidar. *Photonics* **2023**, *10*, 970. <https://doi.org/10.3390/photonics10090970>

Received: 20 June 2023

Revised: 20 August 2023

Accepted: 21 August 2023

Published: 24 August 2023



Copyright: © 2023 by the authors. Licensee MDPI, Basel, Switzerland. This article is an open access article distributed under the terms and conditions of the Creative Commons Attribution (CC BY) license (<https://creativecommons.org/licenses/by/4.0/>).

1. Introduction

In non-visible bands (such as the near-infrared band), planar array imaging detectors usually present a low quantum efficiency due to the limited properties of the sensitive materials. As a result, traditional planar array imaging technology is not a feasible solution for imaging [1], while single-pixel imaging is widely used for remote sensing detection, airborne surveillance, target recognition, biomedicine and other fields [2–9] as it uses a single-pixel detector as a photodetector with a wider spectral range and higher quantum efficiency. A highly sensitive photodetector [10], acting as the signal detection unit of the

relational imaging lidar, can convert the detected laser echo signal into an electrical signal and transmit it to the high-speed data acquisition card. It is then preprocessed by the data acquisition card and sent to the computer. The procedure results in a light intensity value that is correlated with the modulated speckle to obtain the image information of the target object. Fast-growing, highly sensitive optoelectronic devices like photomultiplier tubes (PMT) and avalanche photodiodes (APD) [11–13] have greatly improved the resolution and image quality of relational imaging. PMT is a kind of vacuum photodetector with a secondary emission multiplication system based on external photoelectric effect [14], characterized by high current amplification, high signal-to-noise ratio and a higher quantum efficiency in ultraviolet and visible wavelengths. APD is quantum-efficient in near-infrared and infrared bands, and with higher internal gain [15–17] it is easier to encapsulate and integrate. Therefore, APD is the preferred photodetector for NIR single-pixel imaging lidar.

APD is a kind of photodetector based on the principle of internal photoelectric effect. According to the relationship between the breakdown voltage and the input reverse operating voltage, it can be categorized into two modes of operation. When the input reverse operating voltage is higher than the critical breakdown voltage, APD works in Geiger mode and needs to quench and restore the avalanche process through the supported quenching and reading circuit to detect the next single photon, which is mainly used in single-photon counting and extremely weak light intensity detection [18,19]. Under the effect of reverse operating voltage, the intensity of the electrical signal output from the internal gain detection of the linear-mode APD is proportional to the intensity of the received optical signal, so as to receive successive light pulses of very short time intervals. There is no need for an additional quenching process during the two operating cycle intervals, which have better frequency characteristics. This mode is often used in the field of optical communication, laser scanning and the fast detection of small signals [20–22].

Based on this, an encapsulated APD detector was designed in a linear mode by integrating a bare APD tube, a negative temperature coefficient (NTC) thermistor, a thermo-electric cooler (TEC), a bias power circuit, a temperature control circuit and a signal processing circuit, and then verified in a single-pixel imaging lidar system. Each part of the encapsulated detector was tested, respectively. At the same time, the scattered signal from a 10 KHz pulsed laser was used as the signal source in an experimental test system configured in the laboratory to simultaneously measure and process the re-frequency and pulse width of the scattered signal with the APD detector and a commercial Licel detector. It proved that they had a good consistency. In addition, the encapsulated APD detector was then applied to the near-infrared single-pixel imaging lidar system to acquire laser back scattered signals in a real atmospheric environment, further achieving the image restoration of target objects.

2. Single-Pixel Imaging Lidar System and Detector Circuit Design

2.1. Single-Pixel Imaging Lidar System

Figure 1 illustrates the schematic structure of the near-infrared single-pixel imaging lidar system. The pulsed laser beam emitted by the laser was scanned out through the two-axis galvanometer, and then transmitted horizontally into the atmosphere after the beam was expanded and irradiated to the target object at the distance L . The echo signals scattered in the atmosphere and reflected by the target object on the optical transmission path were collected by the telescope and transmitted to the space light modulator (DMD). Then, the DMD was pre-set with a series of deterministic orthogonal Hadamard-based projection speckles in advance to modulate the echo signal. The modulated signal was focused on the APD detector through a convergent lens and narrow band filter. As such, photoelectric conversion was completed. The converted voltage signal was collected and preprocessed by the high-speed data acquisition card and sent to the computer. The final light intensity value obtained was correlated with the modulated speckle to obtain the imaging information of the target object. Signals between the pulse laser, DMD and data acquisition card were controlled synchronously by the control unit through a sequential control circuit. According to the basic principle of single-pixel imaging [23,24], the target

image was set as $O(x, y)$, and the n th light intensity value obtained by the APD detector and the corresponding Hadamard-based modulated speckle as I_n and $H_n(x, y)$, respectively, so these indicators satisfied

$$I_n = \sum H_n(x, y)O(x, y) \quad n = 1, 2, 3 \dots N \tag{1}$$

where x and y represent the number of pixels on the horizontal and vertical dimensions in the two-dimensional space, respectively, so the image resolution is $x \times y$, and N is the total number of modulated speckles. The image of the target object O_{SPI} could be restored through a relation operation of the Hadamard-based modulated speckle and the obtained light intensity distribution:

$$O_{SPI} = \langle H_n I_n \rangle \tag{2}$$

where $\langle \cdot \rangle$ denotes the set average and can be expressed as $\langle H_n \rangle = \frac{1}{N} \sum_{n=1}^N H_n$, $\langle I_n \rangle = \frac{1}{N} \sum_{n=1}^N I_n$.

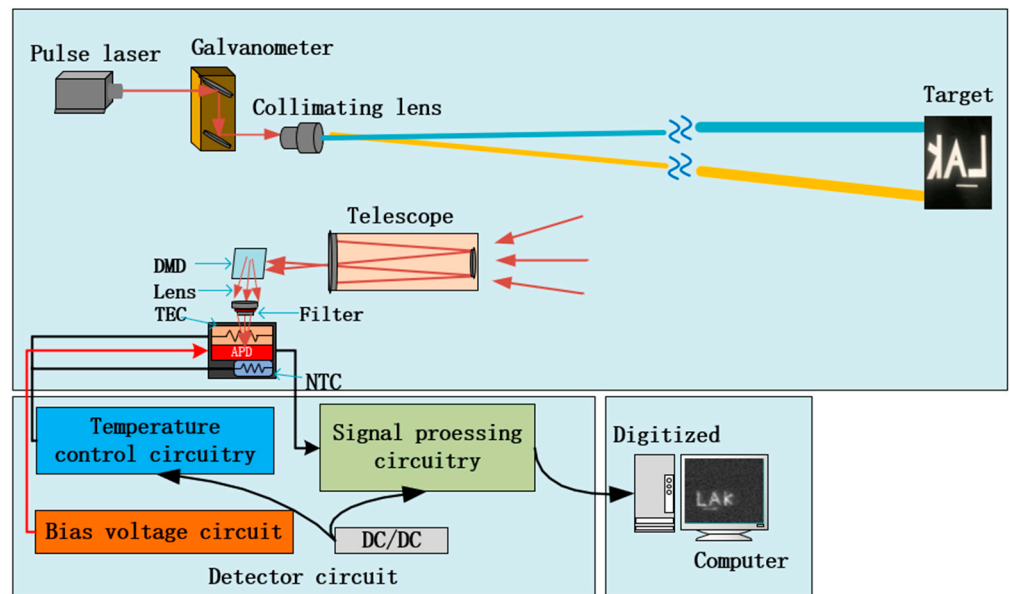


Figure 1. Schematic diagram of the NIR active relational imaging lidar system.

The signal detection unit is a crucial component of the single-pixel imaging lidar system. In order to obtain laser backscattered signals with high sensitivity and signal-to-noise ratio and improve the resolution of single-pixel imaging images, the packaged APD detector should have high quantum efficiency, high gain and bandwidth, and low noise in the 1064 nm band. This paper utilized the AD40000-10 produced by First Sensor, consisting of a 4000 um photosensitive surface, a typical breakdown voltage of 300 V and a spectral response range of 500–1100 nm. It adopted a TO8S package structure with a diameter of ϕ 15.25 mm, and its main parameters are shown in Table 1.

Table 1. Main parameters of AD40000-10 APD.

| Symbol | Characteristic | Test Condition | Min. | Type | Max. | Unit |
|--------|-------------------|---|------|-------------|------|------|
| | Active area | | | Φ 4000 | | um |
| I_D | Dark current | M = 100 | | 50 | 500 | nA |
| C | Responsivity | M = 100; $\lambda = 1064$ nm | | 49 | | A/W |
| t_R | Rise time | M = 100; $\lambda = 1064$ nm; $R_L = 50 \Omega$ | | 6 | | ns |
| t_R | Cut-off frequency | -3 dB | | 70 | | MHz |
| V_b | Breakdown voltage | $I_R = 2$ uA | 200 | 300 | 600 | V |

Laser echo signals were received and converged by the telescope to the photosensitive surface of the APD detector, converted by the APD detector and then transmitted to the acquisition unit as electrical signals. The upper left part of Figure 2 shows the working principle of the bias power circuit, which mainly consists of the LT3757 generating the pulse regulation drive controller (PWM) signals to control the on/off of the MOSEFET tube, indirectly controlling the output high voltage of the transformer and then providing the reverse bias voltage for the APD after passing through the filter circuit to put it in the linear mode. The mid-section of Figure 2 is the temperature control circuit, which operates on the principle that the NTC senses the ambient temperature of the APD. The temperature control circuit converted it to its own resistance value, converted the value into a voltage signal by dividing the voltage through the balanced bridge, and then compared it with the set reference voltage using the differential operational amplifier. The PID control network, which consisted of the capacitance circuit and the operational amplifier, compensated for the resulting error signal. The final pulse regulation drive controller generated a corresponding PWM signal to control the Metal Oxide Semiconductor Field Effect Transistor (MOSFET) shutdown, and exploited the H-bridge (composed of four MOS tubes) to drive the TEC for cooling or heating, thereby automatically controlling the APD ambient temperature through the temperature control circuit. The rightmost part of Figure 2 shows the signal processing circuit. Under the action of bias voltage, laser echo signals were received by the APD and converted into current signals, and converted into voltage signals by TIA. After processing by the secondary main amplifier and filter, the voltage signals were output into the voltage that could be captured by the acquisition card. Detection sensitivity and quantum efficiency were among the important parameters of the signal detector that directly affected the resolution and quality of single-pixel imaging. Not only that, the detection sensitivity was frequently linked to the internal gain M of the APD and the amplification factor of the signal processing circuit. The relationship between the internal gain M and the reverse operating voltage can be expressed as follows:

$$M = \{1 - [(V - I_M R_i)/V_b]^a\}^{-1} \quad (3)$$

where V is the actual reverse operating voltage, I_M the average value of the multiplied output stream, R_i the internal resistance of the APD, V_b the breakdown voltage and a the parameter related to the APD material, doping characteristics and wavelength. The amplification factor of the signal processing circuit was then subjected to the gain bandwidth product of the operational amplifier and the system bandwidth. In addition, changes in the ambient temperature of the APD also directly altered the APD breakdown voltage, quantum efficiency, dark current and other parameters [25], further reducing the APD sensitivity and the stability of the system.

2.2. Detector Circuit

(1) Bias Power Circuit

The intensity of an “avalanche effect” is determined from the reverse operating voltage input to the APD through the bias power circuit power circuit. Therefore, only when the internal gain M was stabilized while the stability and power consumption of the biased power supply were considered could the reverse operating voltage in a linear mode be satisfied. In the present study, a LT3757 booster chip produced by Linear Technology Corporation was selected and configured as the flyback converter [26–29], and a peripheral circuit was built based on this to design the bias power circuit.

As illustrated in Figure 3, when the PWM signal output from the GATE pin was at a high current level, MOSFET Q was in conduction, and the input energy was stored in the primary coil of the transformer, with a current of I_p . At this time, the input energy could not be transferred to the secondary coil due to the cutoff of rectifier diode D, so the capacitor C was discharged from the load, as shown in Figure 4a. When the PWM signal output was at a low voltage level, MOSFET Q was off but the rectifier diode D was on, and

the secondary coil output voltage to the load after being filtered by capacitor C, as shown in Figure 4b. In the meantime, a set of resistance dividers were extracted from the power supply V_{in} to drive the Undervoltage-Lockout (UVLO) of booster chip power, and to finally complete the sequencing or start the over current protection. The output voltage value V_{out} of the bias power circuit could be represented by VR , R_7 and R_8 , as follows:

$$V_{out} = 1.6 \times \left(1 + \frac{VR + R_7}{R_8} \right) \tag{4}$$

where V_{out} stands for the actual output voltage, VR for the adjustable resistor and R_7 and R_8 for the fixed resistors.

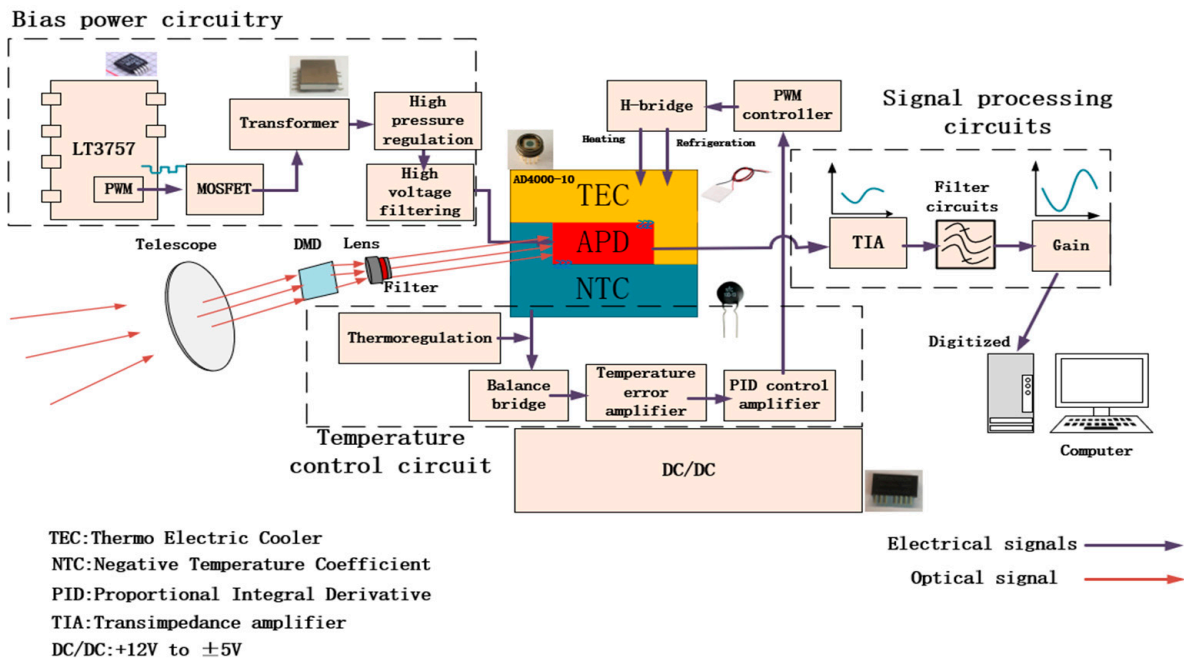


Figure 2. Block diagram of the hardware structure of the APD detector.

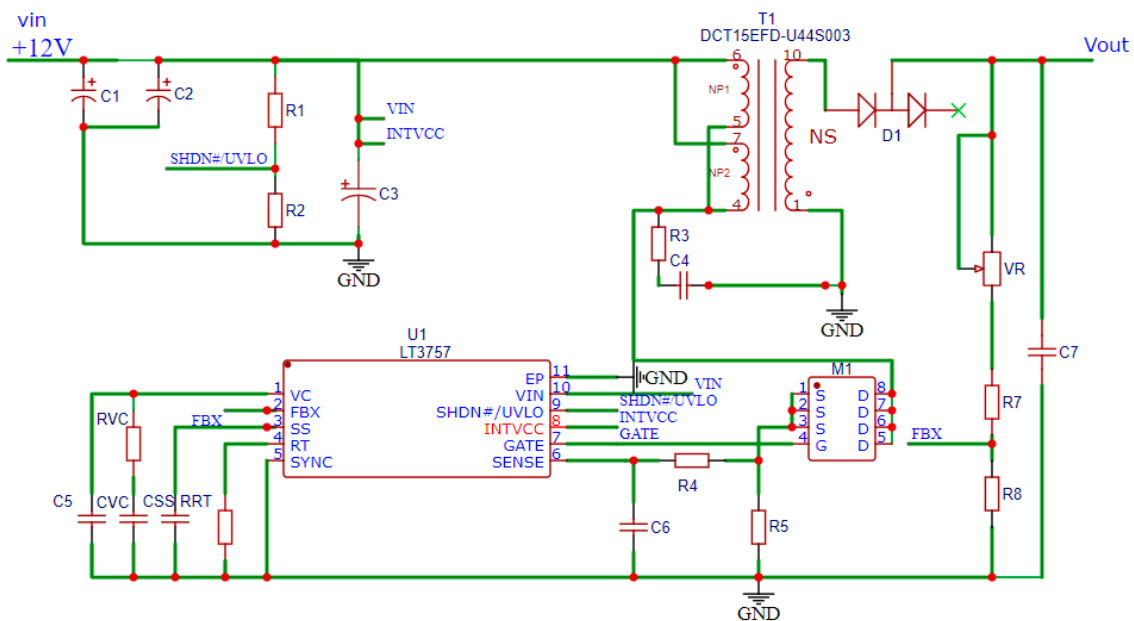


Figure 3. Flyback bias power circuit based on LT3757.

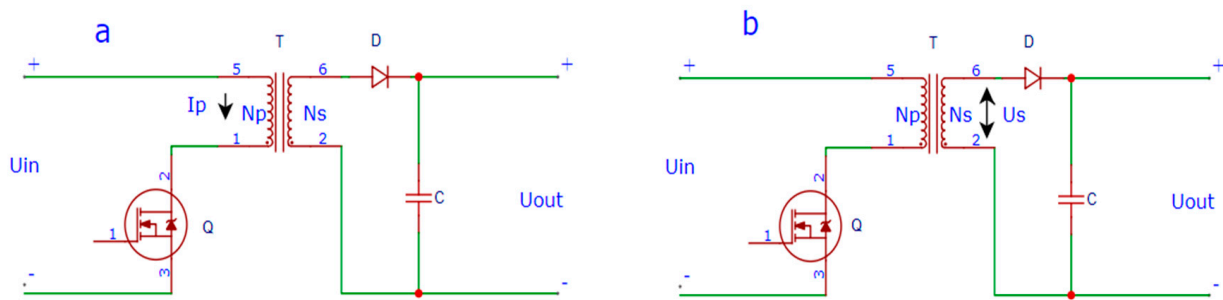


Figure 4. (a) On-state of MOSFET. (b) Off-state of MOSFET.

(2) Temperature Control Circuit

The NTC and TEC integrated in the bare tube of the APD formed a “sandwich” structure close to the APD. The temperature control circuit sensed the ambient temperature of APD through NTC and then formed a balance bridge along with the resistors R and R_X . The voltage signal obtained from the balanced bridge was compared with the set reference voltage by means of a differential operational amplifier. By using resistance capacitance circuits $Z1$ and $Z2$, as well as the operational amplifier, a PID control network was created to compensate for the resulting error signal. Finally, PWM generated the corresponding signal to control MOSFET shutdown, and the H-bridge was utilized to drive TEC cooling or heating, thus realizing the automatic control of the APD ambient temperature, as shown in Figure 5.

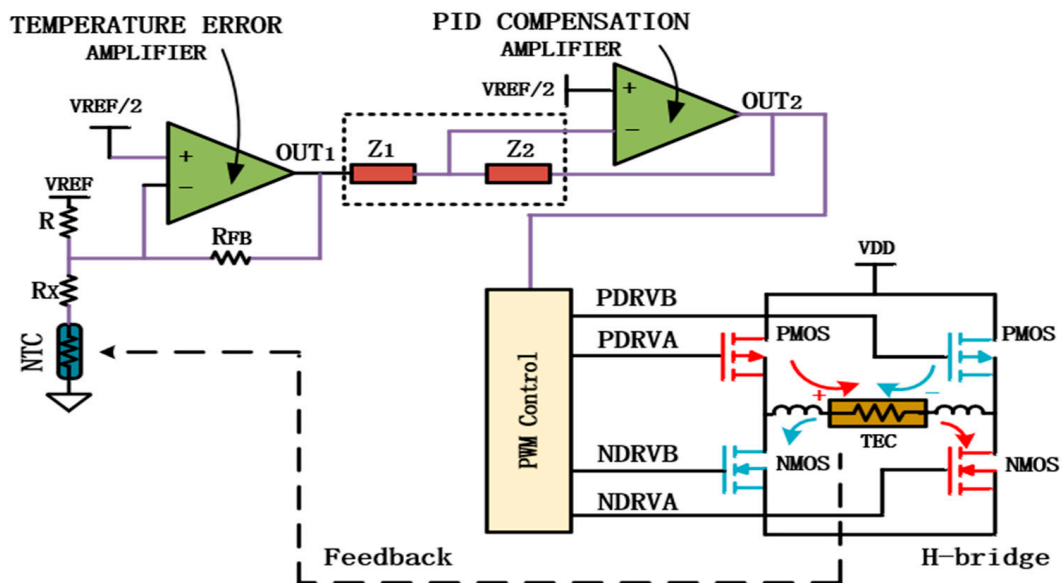


Figure 5. The work principle diagram of temperature control.

(3) Signal Processing Circuit

After photoelectric conversion, the laser echo optical signal detected by APD flowed out of the anode of APD in the form of current, which was weak to about the nA level and needed further amplification. The OPA657 chip with a gain bandwidth of 1.6 GHz from Texas Instruments was regarded as the trans-impedance preamplifier, since it was more suitable for amplifying and transmitting weak signals due to its extremely low input voltage noise, bias voltage and bias current. The trans-impedance amplifier (TIA) converted the current signal from the anode of the APD into a voltage signal. The conversion gain depended on the feedback resistance R_f , but too large an R_f value would cause the shunt stray capacitance to dominate the bandwidth of the circuit. With that, a feedback capacitor

was needed to reduce the high-frequency noise gain of the circuit and prevent the circuit from self-excitation. The post-amplifier circuit was designed with two ADA4899-1 cascaded structures. Meanwhile, a high-pass filter composed of an RC network with a high-pass cutoff frequency of 100 Hz was used to connect the two cascades in order to suppress the interference of low-frequency noise.

Finally, the gain of the signal processing circuit was set to 79.08 dB and the bandwidth to 40 MHz. The signal processing topology was shown in Figure 6.

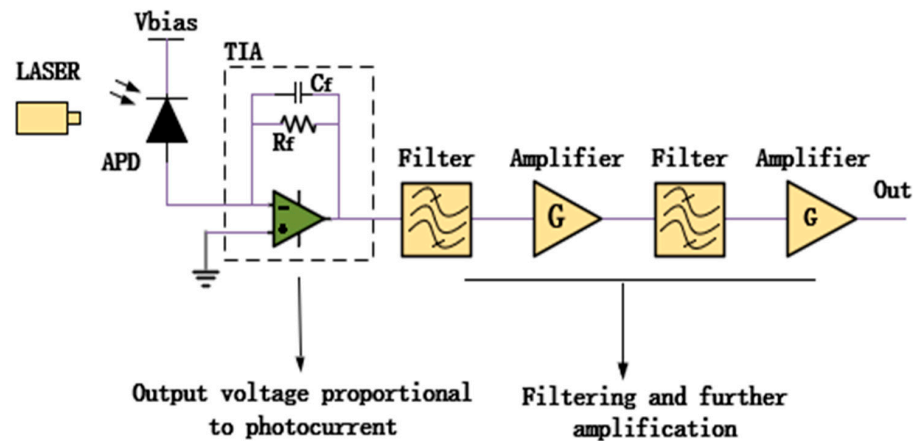


Figure 6. Signal processing topology.

3. Results and Analysis

3.1. Circuit Design Test and Analysis

(1) Bias Power Test and Analysis

The relationship between the output voltage of the designed bias power circuit and Res ($Res = VR+$) resistance was simulated for analysis on the LTspice platform, a circuit simulation software developed by Linear Technology, an American chip manufacturing company. While other parameter values remained unchanged, the resistance range was set between 1.6 KΩ and 2984 KΩ with a step length of 500 KΩ to scan the parameter Res. As seen in Figure 7, the output voltage of the bias power circuit increased as the Res resistance of the power circuit rose, which was consistent with the theoretical calculation results. Also, the obtained output voltage ranged from DC 1.76 V to 300 V. In order to test the stability of the output voltage, the output ripple value was measured by the Tektronix TBS2000x digital storage oscilloscope when the actual output DC was 140 V, 180 V and 220 V, as shown in Figure 8. The actual output transient voltage ripple was less than 0.01% of the output voltage, satisfying the requirements of most APDs for the voltage ripple.

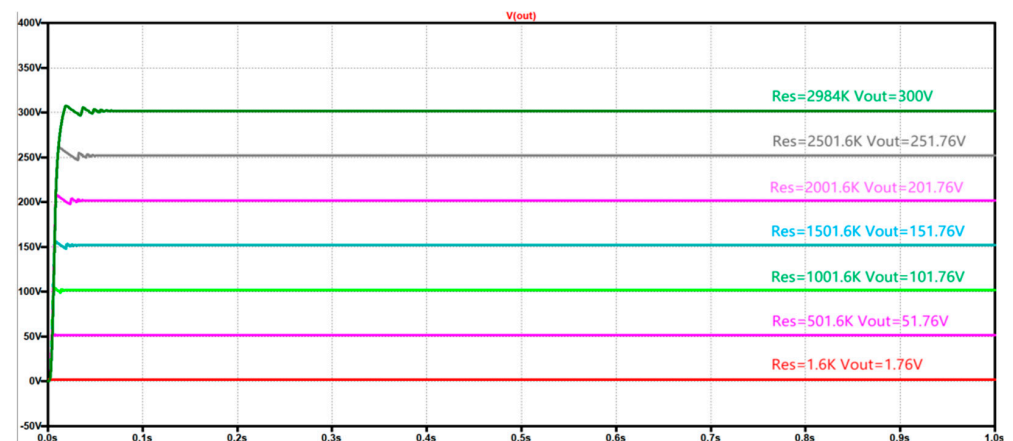


Figure 7. Simulation results of the bias power circuit.

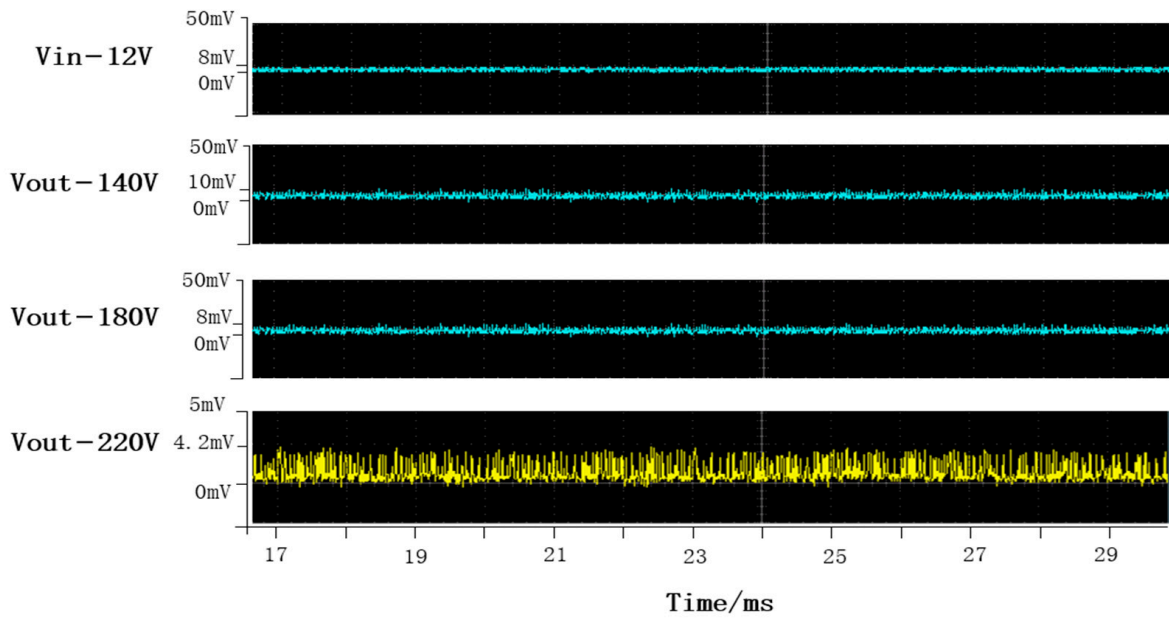


Figure 8. Transient voltage ripple of the bias power circuit at different outputs.

(2) Temperature Control Test and Analysis

In order to verify the maintenance effect of the designed temperature control circuit on the APD ambient temperature, the encapsulated APD detector was placed in a 45 °C incubator environment, and the control temperature of the temperature control circuit was set to 25 °C. At the same time, a stable laser light source with a wavelength of 1064 nm was used to shoot on the APD sensitive surface. The NTC pin was drawn out to the external temperature display module, the APD ambient temperature on the surface was recorded every 2 s, and its time-dependent curve was made within 10 min (shown in Figure 9). In the upper right corner of the figure, a small resolution of temperature changes within 4 min to 6 min was inserted to show the changes in the APD ambient temperature in detail. Among them, the fluctuation of the control temperature resulted from the thermal inertia of NTC material itself [30,31]. At the same time, when selecting the resistance capacitance of the PID compensation network, the value of resistance capacitance could not be accurate to the theoretical calculation value, resulting in certain errors in temperature control. The final temperature control circuit stabilized the ambient temperature of the APD, maintaining 25 ± 0.3 °C within 5 h.

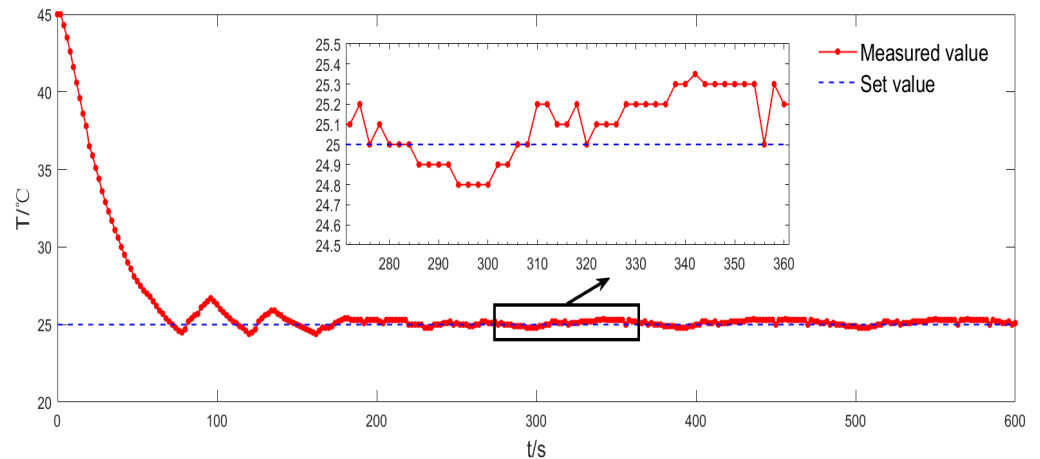


Figure 9. APD ambient temperature curve.

3.2. Detector Test and Analysis

In order to test the performance of the encapsulated APD detector, the pulse laser scattering light signal was used as the signal source in the laboratory.

As illustrated in Figure 10, the test was performed as follows: the laser emitted a pulsed beam with a wavelength of 1064 nm and a repetition rate of 10 KHz to irradiate the target scatterer at a distance of 5 m. The back-scattered signal was incident on the APD photosensitive surface, processed by the encapsulated APD detector, and then displayed and detected by the oscilloscope to obtain its signal information. The results were compared with those of a commercial Licel detector (model C12702-04 APD) under the same experimental environment, and Table 2 shows the main parameters of the Licel detector (model C12702-04 APD). The comparison found that both the encapsulated APD detector and the commercial Licel detector were able to respond to the back-scattered light signal, with a final response frequency of 9.92 KHz. The detection frequency was inconsistent with the calibration frequency of the laser because the laser leveraged the activated medium placed in the optical resonator to generate laser oscillation. Any change in the mechanical length I in the cavity or the refractive index M of the medium between the cavity lenses would result in a frequency variation, due to temperature changes, mechanical vibration and magnetic field change, among other factors [32]. Figure 11 (below left) offers the frequency response results of the encapsulated APD detector and the commercial Licel detector, while Figure 12 (below right) presents their pulse response results. It can be seen that the pulse width of both detectors was about 25 ns when the oscilloscope operated at a scanning speed of 200 ns, accounting for about 5/8, which was related to their design bandwidth. From Figure 12, it can be further seen that saturation distortion occurred when the commercial Licel detector detected a close target due to its fixed gain, and it directly decreased the accuracy of the detection results. The packaged APD detector, on the other hand, had an adjustable gain and was not subject to any distortion at the same distance. This further demonstrated the reliability of the encapsulated APD detector and thus proved its possibility for application in NIR-correlated imaging lidar systems.

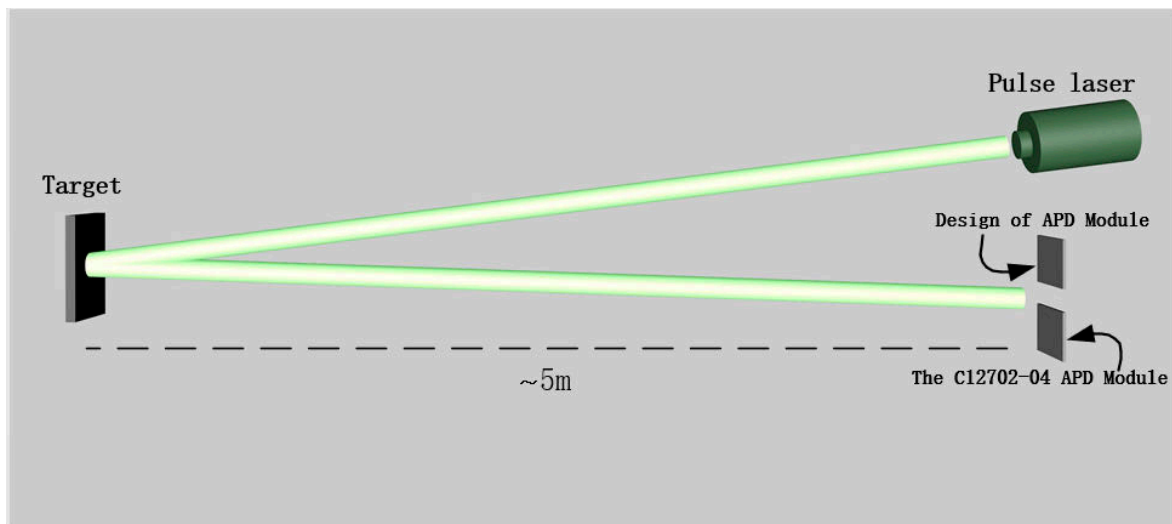


Figure 10. Experimental test of packaged APD detector and commercial Licel detector.

Table 2. Main parameters of the commercial Licel detector (model C12702-04 APD).

| Type No. | Photosensitive Area | Supply Voltage | | | Spectral Response Range | Frequency Bandwidth −3 dB |
|-----------|---------------------|----------------|------|-------|-------------------------|------------------------------|
| | | Min. | Typ. | Max. | | |
| C12702-04 | Φ 3.0 mm | +4.75 | +5 | +5.25 | 400 to 1100 (nm) | 4 kHz–80 MHz |

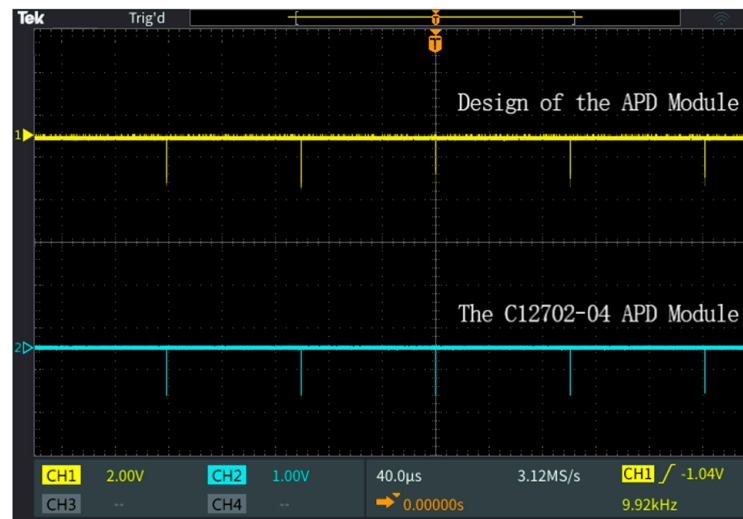


Figure 11. Frequency response of encapsulated APD detector and commercial Licel detector.

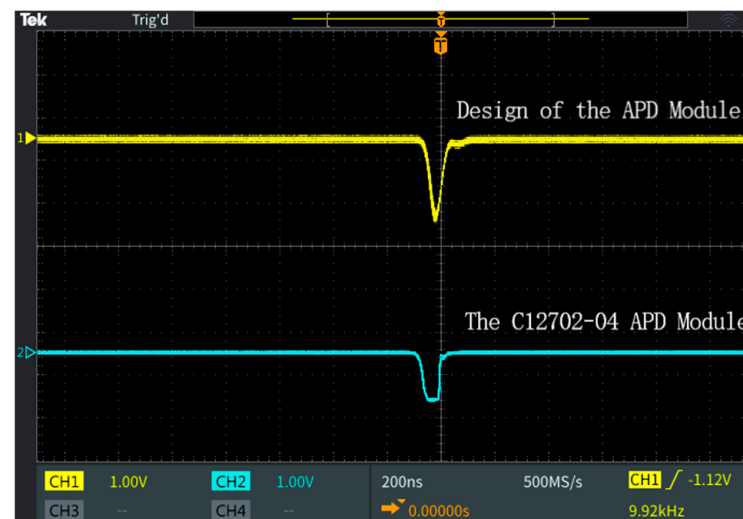


Figure 12. Impulse response of encapsulated APD detector and commercial Licel detector.

For experimental detection under the real atmospheric environment, the encapsulated APD detector was applied to the near-infrared single-pixel imaging lidar system to further test its stability and reliability, as shown in Figure 1. Table 3 provides the technical parameters of each component of the system. Among them, the laser wavelength of the transmitting unit was 1064 nm, the pulse repetition frequency was 400 Hz, the maximum light output energy was 400 mJ, the telescope aperture of the receiving unit was 240mm, the image array of the DMD modulator was 1920 × 1200 and the sampling frequency of the high-speed digital data acquisition card of the signal acquisition unit was 400 MHz. Using a sequential control circuit, the control unit synchronously controlled signals between the pulse laser, DMD and data acquisition card [33,34]. Figure 13a is the layout of the experiment scene. Inserted in the lower left corner of Figure 13a is the imaging target captured with the DSLR camera, a letter puzzle placed about 1.1 km away from the transmitting end of the laser. As shown in Figure 13b, the letters L, A and K were arranged on the same plate, with a thin “one” on the lower right corner, perpendicular to the laser spot. Figure 13c is the distance-dependent formation of echo signals obtained by the APD detector after the laser was scattered in the atmosphere and reflected by the target object, in which the ordinate represented transmission distance, and the ordinate was the intensity amplitude of echo signals. Compared with a weakly scattered signal in the atmosphere, a strong echo signal was detected at a location near 1.1 km. Based on Formulas (1)–(2), the image recovered via

relational calculation was shown in Figure 13d. It can be seen that the three letters L, A and K and the picture “one” were well restored by ignoring high-frequency noise points, indicating that the encapsulated APD detector could realize the active imaging detection of target objects well.

Table 3. Technical parameters of the NIR relational imaging lidar system.

| Section | Parameter | Numeric Value | Section | Parameter | Numeric Value | |
|-----------------------|----------------------------------|-----------------------------------|-------------------------|-----------------------------------|-------------------------------|---|
| Laser emission unit | Laser line | $\lambda = 1064 \text{ nm}$ | Signal acquisition unit | High-speed digital card/bandwidth | 400 MHz | |
| | Pulse repetition frequency | 400 Hz | | Control unit/procedure | DMD pattern | - |
| | Maximum pulse energy | 400 mJ | | | Galvanometer acquisition card | - |
| Signal reception unit | Galvanometer scanned area | $\pm 0.393 \text{ rad}$ | | Synchronizing signal... | - | |
| | Telescopic aperture/focal length | $\Phi = 240 \text{ mm}$ 730 mm | | | | |
| | DMD mirror array /dimension | 1920 × 1200 20.7 × 13.5 mm | | | | |

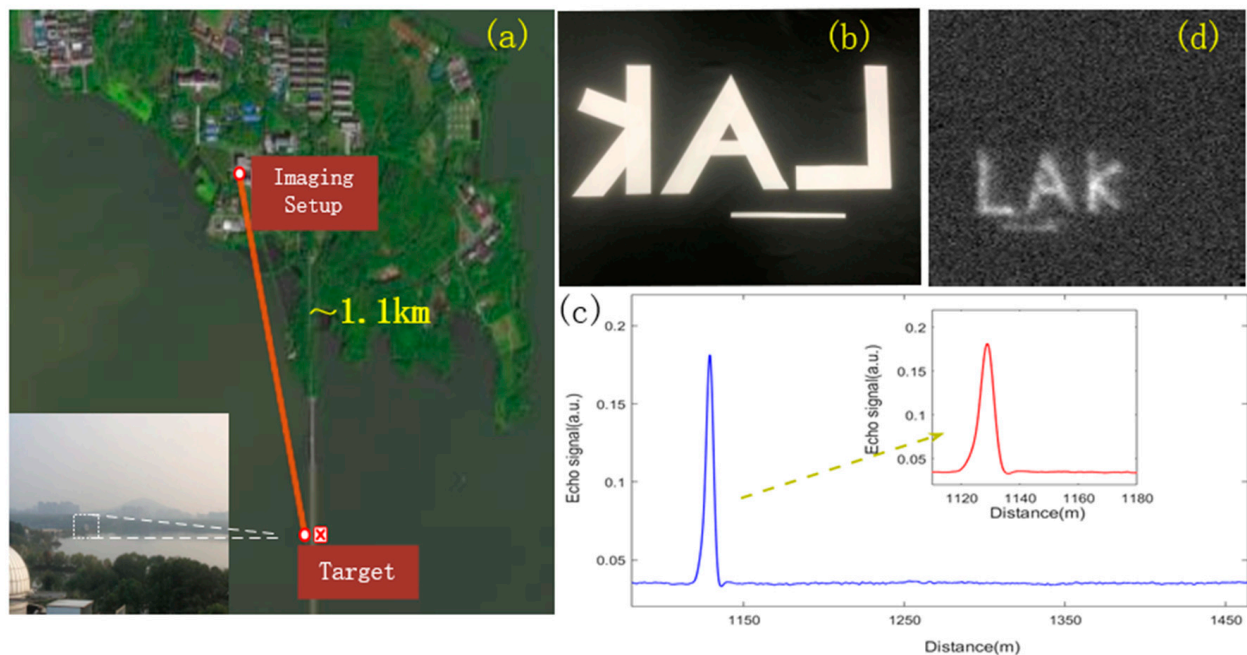


Figure 13. (a) Experimental scene layout. (b) Imaging object. (c) The distribution of the echo signal obtained by the APD detector with distance after the laser has been scattered by the atmosphere and reflected by the target object. (d) Image recovered through relational calculation.

4. Conclusions

With high quantum efficiency in the near-infrared band, APD is often used as the signal detector for lidar. At present, most of the required high sensitivity, low noise APD detectors are imported at high prices, because the domestic development of APD detectors is still in its infancy. Therefore, an integrated encapsulation structure of an APD detector in linear mode was designed and completed in this present study to obtain laser back-scattered signals with a high sensitivity and signal-to-noise ratio, and to improve the image resolution and imaging quality of single-pixel imaging. It integrated a bare APD tube, a negative temperature coefficient thermistor, a semiconductor cooler, a bias power circuit, a temperature control circuit and a signal processing circuit. The performance of the encapsulated APD detector was tested by building an experimental system. The results were as follows:

- (1) The bias voltage circuit was simulated and tested through circuit simulation software, suggesting that the output voltage ranged from DC 1.76 V to 300 V. When the actual output DC was 140 V, 180 V and 220 V, the output transient voltage ripple was less than 0.01% of the output voltage, which satisfied the voltage ripple requirement of most APDs.

- (2) The temperature control unit sensed the ambient temperature of APD through NTC, the differential operational amplifier and PID network compensated the temperature error, and the pulse regulation drive controller changed the TEC working mode, making the ambient temperature stable at 25 ± 0.3 °C within 5 h and eliminating the effects of temperature drift on APD breakdown voltage, quantum efficiency, dark current and other parameters.
- (3) The signal processing unit was designed with a multi-cascade amplification cascade structure to convert and amplify weak signals. The filtering circuit between two cascades effectively filtered out the interference brought by noise and improved the signal-to-noise ratio of the detector.
- (4) In the test experiment carried out in the laboratory with the light scattering signal of the pulsed laser as the signal source, the encapsulated APD detector was in good agreement with the commercial Licel detector on the heavy frequency and pulse width response of the scattering signal.
- (5) The encapsulated APD detector was applied to a near-infrared single-pixel imaging lidar system in the real atmospheric environment, and a laser backscattered signal of 1.5 km was obtained. The imaging experiment was carried out on the letter puzzle target about 1.1 km away from the laser transmitting end, and the target image was recovered by utilizing the basic principle of single-pixel imaging, which further verified the stability and reliability of the encapsulated APD detector by comparing with the physical image.

Author Contributions: Conceptualization, A.L. and K.Y.; methodology, A.L. and K.Y.; software, A.L. and J.H.; validation, A.L., S.Z., Y.C. and Z.H.; formal analysis, A.L. and K.Y.; investigation, A.L. and K.Y.; resources, A.L., K.Y. and Y.C.; data curation, A.L. and J.H.; writing—original draft preparation, A.L.; writing—review and editing, A.L. and K.Y.; visualization, A.L. and J.H.; supervision, K.Y. and D.S.; project administration, K.Y., J.H. and D.S.; funding acquisition, K.Y., J.H. and D.S. All authors have read and agreed to the published version of the manuscript.

Funding: Supported by the Open Project of Advanced Laser Technology Laboratory of Anhui Province (No. AHL2021ZR01); the HFIPS Director's Fund, Grand No. YZJJ202303-TS; the National Natural Science Foundation of China (No. U20A20214); and the Youth Innovation Promotion Association of the Chinese Academy of Sciences (No. 2020438).

Institutional Review Board Statement: We choose to exclude this statement because the study did not require ethical approval.

Informed Consent Statement: The study did not involve humans.

Data Availability Statement: The data presented in this study are available on request from the corresponding author.

Conflicts of Interest: The authors declare no conflict of interest.

References

1. Tian, Z.; Yang, G.; Zhang, Y.; Cui, Z.; Bi, Z. A range-gated imaging flash LiDAR based on the adjacent frame difference method. *Opt. Lasers Eng.* **2021**, *141*, 106558. [[CrossRef](#)]
2. Schwarz, B. Mapping the world in 3D. *Nat. Photon* **2010**, *4*, 429–430. [[CrossRef](#)]
3. Carter, W.E.; Glennie, C.L.; Shrestha, R.L. *Geodetic Imaging by Airborne LiDAR: A Golden Age in Geodesy—A Bonanza for Related Sciences*; Springer: Cham, Switzerland, 2015.
4. Gschwendtner, A.B.; Keicher, W.E. Development of Coherent Laser Radar at Lincoln Laboratory. *Linc. Lab. J.* **2000**, *12*, 383–396.
5. Shi, D.; Huang, J.; Meng, W.; Yin, K.; Sun, B.; Wang, Y.; Yuan, K.; Xie, C.; Liu, D.; Zhu, W. Radon single-pixel imaging with projective sampling. *Opt. Express* **2019**, *27*, 14594–14609.
6. Zha, L.; Shi, D.; Huang, J.; Yuan, K.; Meng, W.; Yang, W.; Jiang, R.; Chen, Y.; Wang, Y. Single-pixel tracking of fast-moving object using geometric moment detection. *Opt. Express* **2021**, *29*, 30327–30336. [[CrossRef](#)]
7. Yang, H.; Fang, Z.; Cao, Y.; Xie, C.; Zhou, T.; Wang, B.; Xing, K.; Lolli, S. Impacts of Transboundary Dust Transport on Aerosol Pollution in the Western Yangtze River Delta Region, China: Insights Gained From Ground-Based LiDAR and Satellite Observations. *Earth Space Sci.* **2021**, *8*, 3. [[CrossRef](#)]

8. Comerón, A.; Muñoz-Porcar, C.; Rocadenbosch, F.; Rodríguez-Gómez, A.; Sicard, M. Current Research in LiDAR Technology Used for the Remote Sensing of Atmospheric Aerosols. *Sensors* **2017**, *17*, 1450. [[CrossRef](#)]
9. Shi, D.; Yin, K.; Huang, J.; Yuan, K.; Zhu, W.; Xie, C.; Liu, D.; Wang, Y. Fast tracking of moving objects using single-pixel imaging. *Opt. Commun.* **2019**, *440*, 155–162. [[CrossRef](#)]
10. Zhang, P.; Zhou, J. Single photon detector and its development. *Sens. World* **2003**, *10*, 6–10. [[CrossRef](#)]
11. Moll, J.L.; Tanenbaum, M.; Goldey, J.M.; Holonyak, N. P-N-P-N Transistor switches. *Proc. IRE* **1956**, *44*, 1174–1182. [[CrossRef](#)]
12. Song, D.; Wang, X. APD, PMT and Hybrid Photodetectors With High-End Sensitivity. *Semicond. Technol.* **2000**, *3*, 5–8+12.
13. Wirth, W.F. High-speed snubberless operation of GTOs using a new gate drive technique. *IEEE Trans. Ind. Appl.* **1988**, *24*, 127–131. [[CrossRef](#)]
14. Fei, W. The Study of Framework of Data Acquisition System for Lidar. Ph.D. Thesis, University of Science and Technology of China, Anhui, China, 2013.
15. Lei, Z. Principle and application of photodetector. *Physics* **1994**, *4*, 220–226.
16. Wu, J.; Yu, X.; Shi, S.; Zheng, L.; Sun, W. Infrared ranging technology by using single photon APD array readout integrated circuit. *Infrared Laser Eng.* **2017**, *46*, 604002.
17. Wang, F.; Tang, W.; Wang, T.; Gou, J. Design of 3D laser imaging receiver based on 8×8 APD detector array. *Chin. Opt.* **2015**, *8*, 422–427. [[CrossRef](#)]
18. Shi, Y.; Zhu, H.; Yang, X.; Zeng, H.; Li, Z.; Liu, C.; Wang, J.; Wang, W. InP-based free running mode single photon avalanche photodiode. *Infrared Laser Eng.* **2020**, *49*, 0103005.
19. Zhang, H.; Wang, L.; Wu, C.; Wang, Y.; Yang, L.; Pan, H.; Liu, Q.; Guo, X.; Tang, K.; Zhang, Z.; et al. Avalanche photodiode single-photon detector with high time stability. *Acta Phys. Sin.* **2020**, *69*, 074204. [[CrossRef](#)]
20. Tao, J. High performance superlattice avalanche photodiodes for ultra-high speed optical communications. *Infrared* **1998**, *7*, 40.
21. Zheng, R.; Wu, G. Pulsed one-dimensional scannerless LiDAR system based on linear APD array. *Infrared Laser Eng.* **2012**, *41*, 96–100.
22. Wang, S.; Sun, H.; Zhao, Y.; Zeng, H.; Liu, T. Method of improving 3D imaging resolution of APD array based on optical phased array. *Infrared Laser Eng.* **2019**, *48*, 406003. [[CrossRef](#)]
23. Sun, M.; Yan, S.; Wang, S. Reconstruction Algorithms for Ghost Imaging and Single-Pixel Imaging. *Adv. Laser Optoelectron.* **2022**, *59*, 0200001.
24. Zhang, Z.; Ma, X.; Zhong, J. Single-pixel imaging by means of Fourier spectrum acquisition. *Nat. Commun.* **2015**, *6*, 6225. [[CrossRef](#)] [[PubMed](#)]
25. Zuo, W.; Zhu, Y.; Qiu, M.; Liu, J.; Chen, W. Influence of performances of APD detector on CO₂ concentration error retrieved by LiDAR measurement. *Infrared Laser Eng.* **2018**, *47*, 406002.
26. Gu, W. Research on Optimization Design and Application of Flyback High Frequency Transformer. Ph.D. Thesis, Nanchang University, Nanchang, China, 2019.
27. Jie, X. Research and Improvement of Cross-regulation Rate of Multi-output Flyback Switching Power Supply. Ph.D. Thesis, Huazhong University of Science & Technology, Wuhan, China, 2019.
28. Wang, Q.; Wang, H.; Tian, H. Design and Simulation of a Flyback Switching Power Supply. *Comput. Simul.* **2021**, *38*, 83–88+138.
29. Zhang, P.; Zhang, L. A Semiconductor Laser's Temperature Control System Based on PID Algorithm. *Electron. Sci. Technol.* **2016**, *03*, 543–545.
30. Liu, F.; Zhang, X.; Jia, Y. Design of closed-loop temperature controlled APD photoelectric detector. *Transducer Microsyst. Technol.* **2016**, *35*, 97–99+106.
31. Li, X.; Peng, H.; Wang, C. APD optimal gain control investigation for spaceborne laser range finder. *Infrared Laser Eng.* **2016**, *45*, 77–82.
32. Huang, J.; Shang, L.; Ma, S.; Zhang, S.; Liu, Q.; Hou, Y.; Kong, Q.; Xu, B. Research Progress on Impact Factors to Output Power of Semiconductor Laser. *Mater. China* **2021**, *40*, 218–224.
33. Huang, J.; Li, Z.; Shi, D.; Chen, Y.; Yuan, K.; Hu, S.; Wang, Y. Scanning single-pixel imaging LiDAR. *Opt. Express* **2022**, *30*, 37484–37492. [[CrossRef](#)]
34. Froehly, L.; Martin, S.N.; Lasser, T.; Depeursinge, C.; Lang, F. Erratum to: “Multiplexed 3D imaging using wavelength encoded spectral interferometry: A proof of principle” [Optics Communications 222 (2003) 127–136]. *Opt. Commun.* **2003**, *224*, 127–136. [[CrossRef](#)]

Disclaimer/Publisher's Note: The statements, opinions and data contained in all publications are solely those of the individual author(s) and contributor(s) and not of MDPI and/or the editor(s). MDPI and/or the editor(s) disclaim responsibility for any injury to people or property resulting from any ideas, methods, instructions or products referred to in the content.